

# ISOPHOTAL STRUCTURE AND DUST DISTRIBUTION IN RADIO-LOUD ELLIPTICAL GALAXIES

G. R. TREMBLAY<sup>1</sup>, M. CHIABERGE<sup>1,2</sup>, C. J. DONZELLI<sup>1,3</sup>, A. C. QUILLEN<sup>4</sup>, A. CAPETTI<sup>5</sup>, W. B. SPARKS<sup>1</sup>, AND F. D. MACCHETTO<sup>1</sup>

*Accepted for publication in ApJ, 17 May 2007*

## ABSTRACT

We investigate isophotal properties and dust morphology in the nuclear regions of 84 radio galaxies, imaged in the optical and near-infrared as part of *Hubble Space Telescope* snapshot surveys. We present a sample-wide trend between host galaxy isophotal structure and the inclination of dusty circumnuclear disks at the centers of 13 of these objects. We find that galaxies containing edge-on disks are invariably seen to possess boxy isophotes, while round, face-on disks are seen exclusively in objects with round or elliptical isophotes. Dust-rich sources with disk-like isophotes are observed only to possess dust in the form of extended filamentary lanes, and not in settled distributions like disks. As we do not expect that edge-on and face-on disks reside in different populations of galaxies, we conclude that perceived isophotal boxiness is dependent upon the angle at which the observer views the host galaxy's axis of symmetry. We discuss our results in the context of dissipative merger scenarios, and infer that dusty disks primarily reside in old, boxy remnants of gas-poor galaxy mergers, whereas filamentary dust lanes reside in younger disk-like remnants of gas-rich mergers.

*Subject headings:* galaxies: active — galaxies: elliptical — galaxies: structure

## 1. INTRODUCTION

Many radio-loud elliptical galaxies possess  $\sim 100$  pc scale distributions of dust and molecular gas, often in settled, disk-like structures surrounding the active galactic nucleus (AGN). While it is widely believed that dusty circumnuclear disks trace accretion reservoirs responsible for feeding the  $\sim 10^9 M_\odot$  black holes at the centers of these objects (e.g., Ferrarese et al. 1996; Jaffe et al. 1996; Ferrarese & Ford 1999), the origin of the dust remains a matter of debate. Were it native to its host galaxy and shed from the envelopes of mature stars, the dust, coupled to the stellar component of its host, should settle into a galactic symmetry plane over the passage of a few hundred Myr. There is a problem with this scenario, however, in that the angular momentum of the stars and dust should then be nearly coincident at all times, though no such correlation has been observed in active or nonactive ellipticals (Goudfrooij 1994, and references therein). This has led to the notion that this dust is external in origin, and likely acquired through a merger, the cooling of hot gas, or tidal stripping from a dust-rich companion (e.g., Goudfrooij & de Jong 1995; van Dokkum & Franx 1995; de Koff et al. 2000; Tran et al. 2001). Dust morphologies other than nuclear disks have also been observed in early-type galaxies, ranging from amorphous clumpy patches to extended filamentary lanes (e.g. Sadler & Gerhard 1985; van den Bosch et al. 1994; de Koff et al. 2000). In the externally-acquired dust scenario, these structures are perhaps snapshots at successive stages of a post-merger dust settling sequence, where clumps diffuse into lanes, and where lanes eventually form nuclear disks, which are thought to be end-stage equilibrium states (Lauer et al. 2005).

Regardless of origin, it is becoming clear that these dust features may act as tracers of the structure, stellar population dynamics, and post-merger histories of their early-type hosts, none of which are particularly well-understood. Elliptical merger remnants, active or otherwise, are far more structurally and kinematically complex than originally thought, and current understanding categorizes early-types into two kinematically distinct schemes (Toomre & Toomre 1972; Searle et al. 1973; Cimatti et al. 2004; Khochfar & Burkert 2005). Elliptical galaxies classified as “disky” tend to be comprised of a rapidly rotating stellar population with an approximately isotropic velocity dispersion, giving rise to the “pointed” shapes of their isophotes. Disky ellipticals tend to be faint with power-law brightness profiles, and comprise two-thirds of the lower end of the elliptical galaxy mass spectrum (Bender, Burstein, & Faber 1992). Conversely, “boxy” ellipticals are characterized by largely anisotropic velocity dispersions, and have been thought of as structurally pressure-supported rather than shaped by stellar rotation, as is the case with disk-like objects. Boxy ellipticals tend to be luminous and massive, with flat core profiles and complex, often triaxial stellar orbits. These properties are thought to give rise to the box-like shape of their isophotes (e.g., Lauer et al. 1995; Faber et al. 1997).

The dramatic disparity between the properties of boxy and disk-like ellipticals suggests that the two classes stem from distinct formation scenarios. This is widely supported by a number of *N*-body simulations of major mergers, which concluded that the formation of either a disk-like or boxy remnant is highly dependent on pre-merger initial conditions, particularly the mass ratio, angular momentum, and dust/gas content of the parent galaxies (e.g., Hernquist 1993; Lima Neto & Combes 1995; Barnes 1996; Bekki & Shioya 1997; Khochfar & Burkert 2005). The general consensus is that, on average, unequal-mass mergers rich in gas and dust (“wet” mergers) produce disk-like early-type remnants, while gas-poor (“dry”) equal-mass mergers of high-density progenitors produce boxy galaxies.

These findings motivate the study of possible connections between dust features and the properties of their underlying starlight distributions, as previous works have

<sup>1</sup> Space Telescope Science Institute, 3700 San Martin Drive, Baltimore, MD 21218; grant@stsci.edu

<sup>2</sup> On leave from INAF—Istituto di Radioastronomia, Via P. Gobetti 101, Bologna I-40129, Italy

<sup>3</sup> IATE, Observatorio Astronómico, UNC, Laprida 854, Córdoba, Argentina

<sup>4</sup> Department of Physics and Astronomy, University of Rochester, 600 Wilson Boulevard, Rochester, NY 14627

<sup>5</sup> INAF—Osservatorio Astronomico di Torino, Strada Osservatorio 20, 10025 Pino Torinese, Italy

done. Tran et al. (2001) studied a redshift-limited sample of 60 dust-rich early type galaxies (31 of which contained dusty disks), finding a high tendency for the major axes of dusty disks to be aligned with their host galaxy isophotal major axes, while there was considerably more spread in the orientation of filamentary lanes with respect to isophotes and no obvious trend. The tendency for dusty disks to align with the host major axis was also observed by Martel et al. (2000) in a study of seven low-redshift radio galaxies containing dusty disks. That work also noticed that face-on disks typically reside in “round” galaxies with very little isophotal boxiness and ellipticity, while edge-on disks show a preference for boxier hosts. However, the small sample size precluded drawing conclusions from this result.

The dust/AGN connection in radio-loud ellipticals is also well studied. Previous works have found a correlation between dust mass and radio emission in these objects (e.g., de Ruiter et al. 2002, and references therein). Furthermore, ongoing examinations of the relationship between radio jets and dusty disks have noted that the majority of jet axes are orthogonally oriented with respect to dusty disk major axes (e.g., Capetti & Celotti 1999; Sparks et al. 2000; Martel et al. 2000). Whether or not this apparent trend is real or simply a result of observational bias (as suggested by more recent works e.g. Schmitt et al. 2002), perpendicular jet/disk orientations are not necessarily expected at  $\sim 100$  pc scales. While the angular momentum of the innermost accreting material should align with the jet and the spin of the black hole (BH), dust well outside the BH sphere of influence (typically of order  $\sim 10$  pc) is dominated by the galactic potential. If this apparent trend is real and not the result of observational bias, these dusty disks may trace possible connections between the structure of galactic equipotentials, the history of the merger that carved them, and the spin of the central BH in active ellipticals.

Whatever the case, the clearly strong motivation for studying dust in radio-loud ellipticals has made for a compelling field of study that has grown over the past decade. Recent *Hubble Space Telescope* (*HST*) near-infrared imaging of a complete sample of 3CR radio galaxies has granted unprecedented views of their elliptical hosts less obscured by extinction from dust (Madrid et al. 2006; Donzelli et al. 2007). This, combined with optical *HST* observations of the same sample, allows us to more closely study connections between the properties of dust features and the structure of the radio galaxy hosts in which they reside. In this paper, we expand upon the findings of Martel et al. (2000), particularly with regards to isophotal structure and the morphology of nuclear dusty disks and lanes. In §2 we describe our sample and associated observations, and in §3 we describe the reduction of this data and the extraction of isophotal profiles, namely those of the fourth Fourier cosine (“boxiness”) coefficient  $a_4/a$  and ellipticity  $\epsilon$ , from the iterative fitting of ellipses to host galaxy isophotes. In §4 we present the results of comparing dust morphology, distribution, and inclination (in the case of dusty disks) to isophotal boxiness and ellipticity, as well as radio fluxes from the core and extended regions of the host. In §5 we discuss the implications of our results in the context of the expression of isophotal boxiness and diskiness in early-type galaxies. We also discuss the possible origins of dusty disks and lanes with regards to merger scenarios. We summarize this work and discuss areas of future study in §6. Throughout this paper we use  $H_0 = 71 \text{ km s}^{-1} \text{ Mpc}^{-1}$ ,  $\Omega_M = 0.27$ , and

$$\Omega_\Lambda = 0.73.$$

## 2. SAMPLE SELECTION AND OBSERVATIONS

Our study is largely based on a complete redshift ( $z < 0.3$ ) and flux-limited sample of Fanaroff & Riley (1974, hereafter FR) class I and II radio galaxies, the majority of which are derived from the extragalactic subset of the Revised Third Cambridge Catalog (3CR; Bennett 1962a,b; Spinrad 1985). 3CR sources are categorized as such given a flux density at 178 MHz exceeding 9 Jy, as well as a location on the sky constrained to declinations  $\delta > -5^\circ$  and galactic latitudes  $b > 10^\circ$ . Observations of radio galaxies at 178 MHz detect extended, unbeamed jet lobes, so the sample is free from orientation bias, making it well-suited to statistical studies of host galaxy properties.

Of the 116 3CR sources with  $z < 0.3$ , our sample is comprised of the 83 for which there is archival near-infrared imaging from *HST*. We also include NGC 6251 in our sample, not part of the original 3CR catalog because of a minor position technicality (Waggett, Warner, & Baldwin 1977). Laing, Riley, & Longair 1983 later included NGC 6251 as part of their complete revised sample (the 3CRR catalog). This brings our sample to a total of 84 targets. As this study aims to compare the morphology of dust features with the isophotal properties of their hosts, we focus primarily on a 33 object dust-rich subset of our sample, identified as such by previous *HST* optical studies (e.g., de Koff et al. 1996; Martel et al. 1999; de Koff et al. 2000). The dust features of NGC 6251 were studied in detail by Ferrarese & Ford (1999), and references therein. We include the 52 remaining dust-poor targets for the purposes of comparing the global isophotal properties of a large number of objects.

We obtain the archival near-infrared (NIR) and optical imaging for our sample, allowing us to capitalize on the varying effects of extinction from dust at these two wavelength regimes. As extinction is reduced at near-infrared compared to optical wavelengths, our analyses of host galaxy isophotal properties are largely based on a near-infrared snapshot survey of 3CR targets at  $1.6 \mu\text{m}$  (similar to *H* band). These observations were performed by the Near-Infrared Camera and Multiobject Spectrograph (NIC2) on board *HST*, under SNAP program 10173 (PI: Sparks, Madrid et al. 2006). The completeness of this program was subject only to the observing schedule of *HST*, and not for any other reason specific to any individual target. This subsample of NICMOS NIR imaging is therefore as bias-free as the 3CR sample itself. For a small number of the objects in our sample, the NICMOS imaging we utilize was taken as part of other programs, the references for which may be found in Table 1.

These data were obtained from the Multimission Archive (MAST) at the Space Telescope Science Institute (STScI), having passed through the *HST*/NICMOS on-the-fly reprocessing (OTFR) pipeline yielding nearly science-ready data. Post-pipeline corrections (i.e., removal of the NICMOS pedestal effect, Noll et al. 2004) were performed by Madrid et al. (2006) and Donzelli et al. (2007), in which more detailed information specific to the NICMOS data reduction can be found. All NICMOS observations presented in this paper had a projected pixel scale of  $0''.075$ , and were performed using the F160W (analog of *H* band) filter over a total exposure time of either 1152 seconds (for all program 10173 targets) or for slightly shorter times (see the references in Table 1 for information specific to these images).

For nearby ( $z < 0.1$ ) galaxies, the *HST*/NIC2 field of view

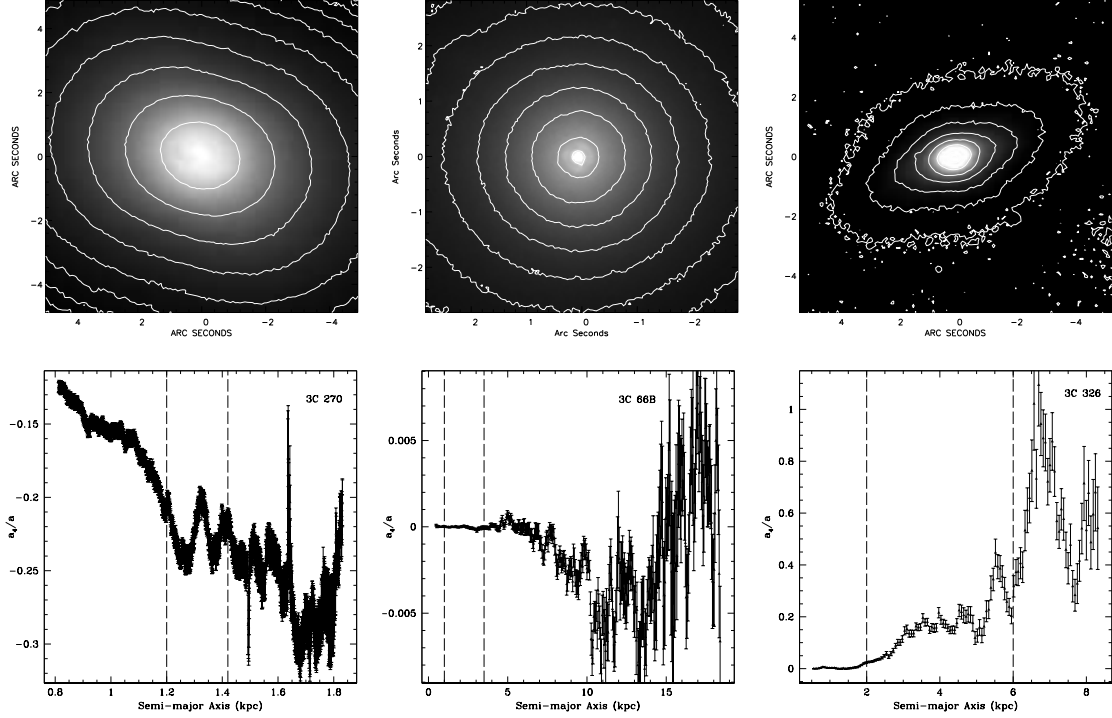


FIG. 1.— Examples of isophotal boxiness in varying degrees. *Left*: *HST*/NIC2 image of 3C 270 at  $1.6 \mu\text{m}$  with highlighted isophotal contours (*top*), its associated  $a_4/a$  profile (*bottom*). Dashed vertical lines indicate the region over which  $a_4/a$  and  $\epsilon$  were averaged for 3C 270. The isophotes of this object are classified as extremely boxy. *Middle*: Same as (*Left*), but for 3C 66B. The isophotes of this object are classified as round. *Right*: Same as (*Left*), but for 3C 326. The isophotes of this object are classified as extremely disk-like.

is prohibitively small and limits our ability to sample near-infrared background levels. We therefore utilize a companion ground-based NIR dataset (Marchesini et al. 2005), obtained with the *Telescopio Nazionale Galileo* (*TNG*). The observations were performed with two *TNG* instruments over two observing runs. In both cases, imaging was performed with filters centered around  $2.12 \mu\text{m}$  ( $K'$ -band) for a typical exposure time of  $\sim 10$ – $20$  minutes, depending on the magnitude of the source. Detailed information regarding the observations is found in Table 3 of Marchesini et al. (2005).

As this paper traces a connection between host galaxy isophotal properties (studied in the near-infrared) and dust content (better observed in the optical), we retrieve archival *HST*/WFPC2 imaging for those 3CR radio galaxies already known to contain dust lanes or dusty disks, as detailed by de Koff et al. (2000). This optical data was retrieved from MAST and sent through the *HST*/WFPC2 OTFR pipeline. As our use for the optical data only extended to the creation of color maps (discussed in §3.2), we were only interested in the dusty central regions of the host galaxy. As such, OTFR calibrated images are adequate for our purposes, and no post-pipeline corrections were necessary. Point-spread function (PSF) differences between the  $R$ - and  $H$ -band data were ignored, as any variation would only strongly affect regions of high surface brightness (e.g., very near the nucleus, which we are not interested in). We were not concerned with optical or NIR nuclei corrupting the natural shape of isophotes or color map isochromes as they are faint throughout our sample. All *HST*/WFPC2 images presented in this paper were taken with the F702W filter (analog of  $R$  band), for which the mean wavelength is  $\langle\lambda\rangle = 6818 \text{ \AA}$ . While one of the most efficient configurations for WFPC2, it also includes in its pass-band contributions from line and continuum emission. At the redshifts considered in this paper, these include  $H\alpha$ , [NII],

and [OIII]. The WFPC2 Planetary Camera has a field of view of  $36''.4 \times 36''.4$  and a projected pixel scale of  $0''.0455$ .

### 3. RADIAL BRIGHTNESS PROFILES: QUANTIFYING BOXY AND DISKY ISOPHOTES

Luminosity profile extraction from the *HST*/NICMOS and *TNG* images via isophotal ellipse fitting was performed by Donzelli et al. (2007) using the IRAF routine ELLIPSE within STSDAS (Jedrzejewski 1987). These fits were performed from the very inner regions of the *HST* and *TNG* images to the outer regions with a count level of  $2\sigma_{\text{sky}}$ . More detailed information regarding these fits, including the masking of dust features and foreground objects, can be found in §4 of Donzelli et al. (2007).

The primary output of ELLIPSE is a table detailing the radial profiles of a number of isophotal parameters (and their associated uncertainties), one of which is the harmonic amplitude  $B_4$ . The standard metric for “boxiness” and “diskiness” in isophotes is the 4<sup>th</sup> order Fourier cosine coefficient  $a_4/a$ , a measurement of isophotal radial deviation ( $a_4$ ) normalized to the semi major-axis  $a$  at which the ellipse was fit.  $B_4$  can be converted to  $a_4/a$  following the convention described by Milvang-Jensen & Jørgensen (1999). That is, ELLIPSE table values of  $B_4$  are normalized to both the equivalent radius  $r = \sqrt{ab}$  (where  $a$  and  $b$  are the isophotal semi-major and semi-minor axes, respectively) as well as the local gradient in intensity  $I$  (also computed from ELLIPSE),

$$a_4/a = \frac{B_4}{r \cdot \left| \frac{dI}{dr} \right|} \cdot \sqrt{\frac{b}{a}}. \quad (1)$$

The extra factor of  $\sqrt{b/a} = \sqrt{1-\epsilon}$  (where  $\epsilon$  is the isophotal ellipticity from ELLIPSE) is needed to re-normalize the radial deviation to  $a$  as opposed to  $r$ , so as to be consistent with the standard in the literature (Bender & Möllenhoff

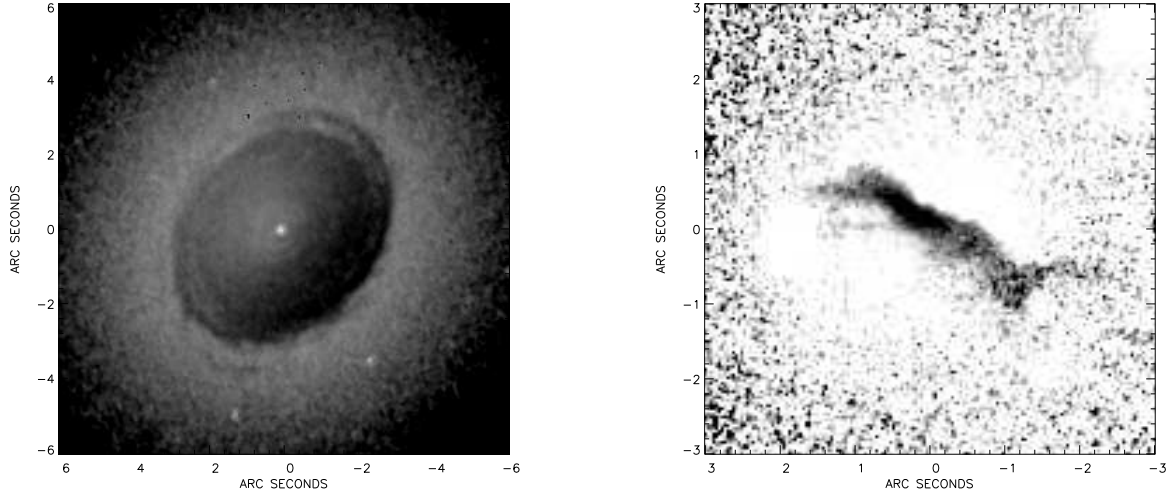


FIG. 2.— Examples of a circumnuclear dusty disk and a dust lane, respectively. (a)  $1.6\ \mu\text{m}/0.702\ \mu\text{m}$  absorption map of the nuclear disk of 3C 31, made from dividing *HST*/NICMOS and *HST*/WFC2 images. The disk exhibits more absorption on its southwestern edge, and previous studies of the axial ratio ( $b/a$ ) for the disk have estimated the southwestern edge to be nearer the observer than the northeastern edge, with  $\arccos(b/a) \approx 41^\circ$  with respect to the plane of the sky (Fraix-Burnet et al. 1991; de Koff et al. 2000) (b)  $1.6\ \mu\text{m}/0.702\ \mu\text{m}$  absorption map of the  $\sim 6.5$  kpc dust lane in 3C 321. Note that, while we include 3C 321 in this figure because it best illustrates what we define as a dust lane, we do *not* include it in our 84 object sample as its *H*-band isophotes are very highly distorted by a foreground object.

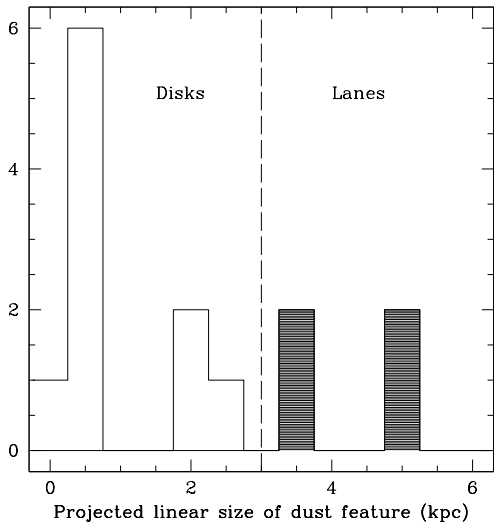


FIG. 3.— Distribution of projected linear sizes of the 17 dusty disks and lanes in our sample. The grey region of the histogram represents dust lanes, the white region indicates that the feature is a disk. See Table 1 for a qualitative classification of dust morphology (where applicable) for every object in our sample.

1987; Milvang-Jensen & Jørgensen 1999). Negative values of  $a_4/a$  indicate that the host’s isophotes are boxy, while largely positive values of  $a_4/a$  are manifestations of disk isophotes. Typically,  $|a_4/a|$  does not exceed  $\sim 0.3$ . An object with values of  $a_4/a \approx -0.2$  is considered extremely boxy (see Fig. 1), and a galaxy whose isophotes have values around  $a_4/a \approx 0.2$  is extremely disk. Objects with  $a_4/a$  values very close to 0 would be described as “elliptical” or “round”, as would be the case for an object with a very small  $a_4/a$  as well as negligible ellipticities  $\epsilon$ .

We define the average  $a_4/a$  of a selected range of a galaxy’s luminosity profile as  $(a_4/a)_{\text{ave}}$ . As this paper places great importance on  $(a_4/a)_{\text{ave}}$  as a physical quantity, we must be careful in how we compute this average. For each object, we plot the radial dependence of  $a_4/a$  and associated errors so as

to judge its behavior at varying galactic radii. Based on these plots, we make a selection for the radial region over which we calculate  $(a_4/a)_{\text{ave}}$  and  $\epsilon_{\text{ave}}$  based on the following *qualitative* constraints:

- The region is sufficiently large (e.g. at least  $\sim 1$  kpc) to ensure that the  $(a_4/a)_{\text{ave}}$  and  $\epsilon_{\text{ave}}$  quantities are generally representative of the host galaxy’s overall isophotal structure.
- In the case of objects with nuclear dust features (e.g. disks) or an unresolved nuclear peak, we are careful to avoid the inner regions of the host, and begin our selection region at least  $2''$  away from the nucleus. This was done for nearly every object in our sample.
- The  $a_4/a$  values within the selected region do not have associated uncertainties greater than the overall errors typical to the fit. While this is a qualitative assessment of error, we strengthen the confidence in our selection by also ensuring that the mean position angle (PA) of each ellipse does not vary greatly throughout the region, and that the  $a_4/a$  profile is relatively stable (i.e. it does not “spike” dramatically within the selection region)

These regions must be selected uniquely for each target, as  $a_4/a$  profiles vary greatly throughout our sample given the effects of redshift, obscuring dust features, foreground objects, close companions, ELLIPSE fit parameters, etc. In general, the regions over which the above requirements were satisfied fell between the isophote  $\sim 1$  kpc from the nucleus and the galaxy’s effective radius (e.g., the radius of the isophote containing half the total luminosity of the host, see Table 1). This averaging strategy is illustrated in Fig. 1, in which we give examples of (from left to right in the figure) very boxy (3C 270), round (3C 66B) and very disk (3C 326) host galaxies, respectively. Alongside the *HST*/NIC2  $1.6\ \mu\text{m}$  isophotal contour plots (top) for these objects, we present the associated  $a_4/a$  radial profiles (bottom) from the ELLIPSE fits. The vertical dashed lines on the plots mark the region over which we calculate  $(a_4/a)_{\text{ave}}$  and  $\epsilon_{\text{ave}}$  values for each host. Eleven of

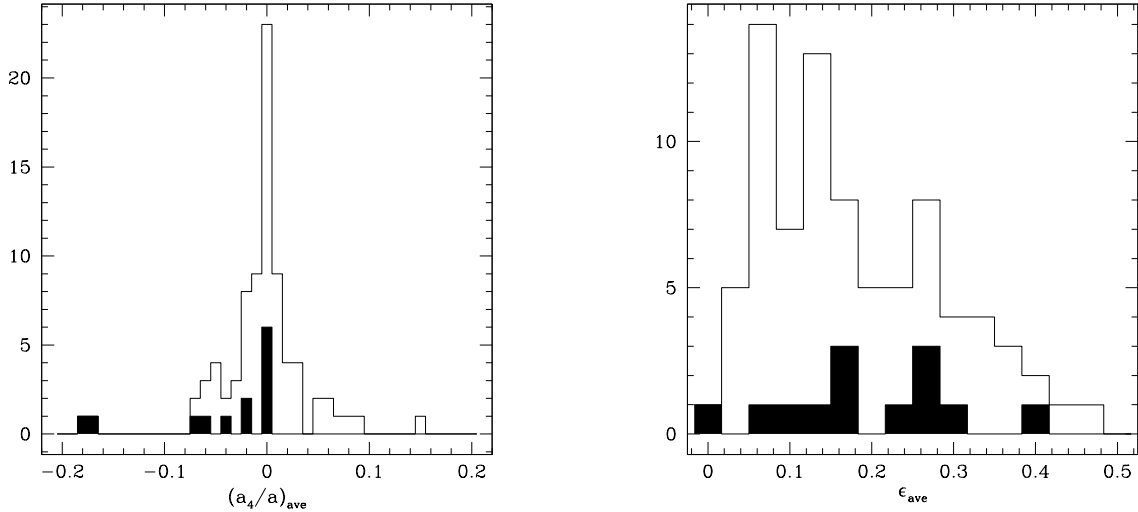


FIG. 4.— (a) Distribution of the  $(a_4/a)_{\text{ave}}$  boxiness parameters for our sample. Shaded parts of the histogram represent the boxiness distribution for objects containing dusty disks. (b) Distribution of mean isophotal ellipticities for our sample, averaged over the same range used to average  $a_4/a$  values. See §3.2 for a discussion of our strategy in selecting these ranges.

our luminosity profiles had associated errors that were higher than the global average error for our sample. Typically, this was due to some observational irregularity, often resulting in the object being close to the NIC2 chip edge. In other cases, large amounts of extinction from dusty clumps and patches impeded our ability to confidently fit the isophotes. While we provide estimated isophotal properties for the majority of these objects, we do not include them in our following global comparisons of isophotal properties. Information specific to the isophotes of every object in our sample may be found in Table 1.

#### 4. RESULTS

##### 4.1. Dusty disks and lanes

Of the 84 galaxies in our sample, we identify 33 with dust in various distributions, including clumpy patches not centered on the nucleus, lanes at kpc scales, and circumnuclear disks hundreds of pc in diameter. We find 13 such dusty disks, clearly resolvable either in optical WFPC2 data or with an  $H/R$ -band color map. Our color maps have been normalized such that a measured difference in pixel values between two regions corresponds to a difference in a proportional number of  $R$ -band magnitudes. This allows for quick extinction estimates.

In Fig. 2a we present our color-map for 3C 31, which contains an excellent example of a dusty disk. Although the largest in our sample (at  $\sim 2.5$  kpc in diameter), this disk shares similar properties with the 12 others we observe. Based on their common traits, we define a dusty disk as a round nuclear feature seen in absorption, qualitatively appearing continuous (from its outer boundaries to the nucleus), flat, and sufficiently resolvable so as to allow for a confident estimate of  $b/a$  (the ratio of the disk’s minor axis  $b$  to its major axis  $a$ ). Assuming a circular, flat disk, this axis ratio can be projected into an estimate for the disk’s inclination  $i$  with respect to the plane of the sky by  $i = \arccos(b/a)$ . These disks are typically associated with more than 1  $R$ -band magnitude of extinction. In many instances, it was necessary to first produce an  $H/R$ -band color map so as to confirm the dust feature was indeed continuous from its outer edge to

the unresolved nucleus. Many of the dusty disks in our sample possess small asymmetries, including lopsidedness (e.g., 3C 465, giving rise to added uncertainty in its  $b/a$  estimate; see Fig. 8), non-planar warps (e.g., NGC 6251, 3C 449, Fig. 8, Ferrarese & Ford 1999; Tremblay et al. 2006), spiral features (e.g., 3C 31, Fig. 2a), and wispy filamentary structures (e.g., 3C 66B). As our study is concerned with the orientations of disks as measured with respect to their *outer* edges, we are generally not concerned with these small-scale features.

In Fig. 2b is a color-map of the highly disturbed dust feature in 3C 321, which we classify as a lane. The three other features defined as lanes in our sample are similar in appearance, being “arc”-like instead of flat like a disk, and are unlikely to extend all the way to the nucleus. Instead, the lanes in our sample appear to reside at much greater distances from the nucleus than do the disks, and the projected extent of a lane is always far greater than a disk diameter. For these reasons, it is not likely that we are misidentifying edge-on disks as lanes. In Fig. 3 we present the distribution of linear sizes for all of the disks and lanes in our sample. Lanes are associated with a swath of extinction (greater than 1  $R$ -band magnitude) spanning more than  $\sim 4$  kpc, while the disks in our sample have diameters smaller than  $\sim 2.5$  kpc.

Some objects in our sample (e.g., 3C 317, 3C 338) contain thin tendrils and wisps of dust, which we do not consider lanes. While lanes are typically associated with more than one  $R$ -band magnitude of extinction, far less massive and cohesive features such as the one in 3C 338 are far more optically thin at  $R$ -band and are better described as “wispy tendrils” or clumps rather than full lanes. We also note that 3C 236 is unique in that its inner dusty disk is connected to a large surrounding filamentary structure. We do not classify this outer feature as a lane as it appears to be connected to the inner disk by a thin tendril. Nevertheless, we measure the inclination of the dust feature in 3C 236 with respect to the *inner* nuclear disk. We discuss 3C 236 further in §6. See Table 1 for a qualitative classification of dust morphology (where applicable) for every object in our sample.

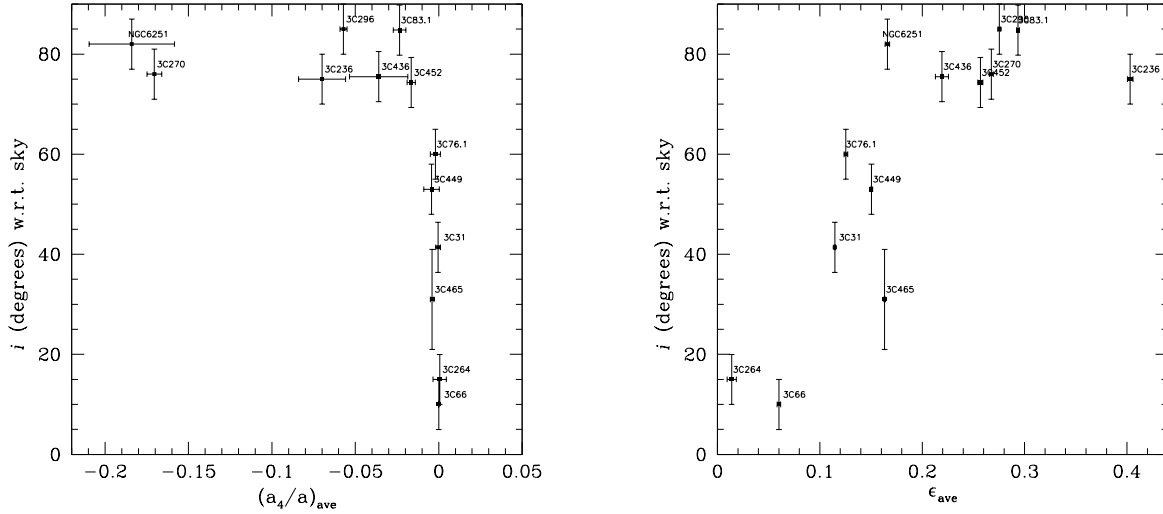


FIG. 5.— (a) Inclination  $i$  (in degrees and with respect to the plane of the sky) of the 13 dusty disks in our sample vs. the  $(a_4/a)_{\text{ave}}$  “boxiness” parameter of their host galaxy isophotes. Dusty disk inclinations  $i$  are estimated for each disk by  $i = \arccos b/a$ , where  $b/a$  is the ratio of the disk’s minor and major axis lengths.  $(a_4/a)_{\text{ave}}$  values are calculated from a region-specific average of  $a_4/a$ , the  $\cos 4\alpha$  Fourier coefficient normalized to the semi major axis of the isophote at which it was measured (see §2). Negative values of  $(a_4/a)_{\text{ave}}$  are indicative of “boxy” isophotes, whereas positive values are manifestation of “disky” isophotes. Note the correlation between disk inclination and isophotal boxiness. (b) Dusty disk inclination  $i$  vs. average isophotal ellipticity  $\epsilon_{\text{ave}}$ . As was the case for boxiness, there also appears to be a relationship between disk inclination and ellipticity.

#### 4.2. Host galaxy isophotal properties

Here we examine the sample-wide distributions of the isophotal parameters  $(a_4/a)_{\text{ave}}$  and  $\epsilon_{\text{ave}}$ , which we calculated using the strategy discussed in §3. The histograms for these distributions are plotted in Figs. 4a and b, respectively. The shaded regions of both histograms mark the 13 objects in which we observe dusty disks, the morphologies of which we describe in §4.1.

From the  $(a_4/a)_{\text{ave}}$  distribution in Fig. 4a, it is clear that our sample favors boxy (e.g.  $-0.1 < (a_4/a)_{\text{ave}} < 0$ ) over diskly (e.g.  $0 < a_4/a < 0.1$ ) objects by one-third to one-quarter of the sample, respectively. Of greater interest is the fact that dusty disks only appear in elliptical (or round) and boxy hosts (e.g., with negative values of  $(a_4/a)_{\text{ave}}$ ), and are not observed in diskly objects (with  $a_4/a > 0$ ) at all. The distribution of mean ellipticities shown in Fig. 4b is decidedly flatter than the spread in  $(a_4/a)_{\text{ave}}$ , and is representative of a wider range of intrinsic ellipticities observed in active and nonactive ellipticals.

The most significant result here is that dusty disks are not found in diskly galaxies. We expand upon this finding in the following section, in which we examine possible connections between the inclinations of these disks and the specific  $(a_4/a)_{\text{ave}}$  values of the boxy hosts in which they reside.

#### 4.3. A trend in dusty disk inclination and isophote boxiness

Here we compare isophotal boxiness to dust morphology for those objects observed to contain nuclear disks. In §4.1, we described how we estimate the inclinations of these disks with respect to the plane of the sky. We plot these inclinations vs. the calculated  $(a_4/a)_{\text{ave}}$  of their host galaxies in Fig. 5a. Despite the inherent uncertainties, this plot brings to attention several interesting properties.

As was the case for Fig. 4a, we see again in Fig. 5a that no circumnuclear disks are observed in diskly host galaxies. More specifically, these disks reside exclusively in host galax-

ies with  $(a_4/a)_{\text{ave}} < 0$ , ranging from round (i.e., 3C 264) or elliptical (i.e., 3C 449) to boxy (i.e., 3C 296) and very boxy (i.e., NGC 6251).

Moreover, the distribution of these objects appears to follow a trend. While face-on or moderately inclined disks are all clustered very near  $(a_4/a)_{\text{ave}} \approx 0$  with very little spread, nearly edge-on disks are seen only in clearly boxy hosts with  $(a_4/a)_{\text{ave}}$  ranging nearly an order of magnitude in negative values.

Comparing this result to Fig. 5b in which we plot  $\epsilon_{\text{ave}}$  against  $(a_4/a)_{\text{ave}}$ , it is apparent that, at least for the low to moderately inclined disks, ellipticity roughly correlates to inclination. That is, low inclination disks (e.g., 3C 66B, 3C 264, and 3C 76.1) tend to reside in *round* host galaxies with  $(a_4/a)_{\text{ave}} \approx \epsilon_{\text{ave}} \approx 0$ . Moderately inclined disks (e.g., 3C 465, 3C 31, and 3C 449) appear to reside in hosts with *elliptical* isophotes having  $(a_4/a)_{\text{ave}} \approx 0$  and an intermediate or high value of  $\epsilon_{\text{ave}}$ . On the other hand, there is considerably higher spread in  $\epsilon_{\text{ave}}$  for the highly inclined, boxy galaxies. NGC 6251, for example, is by far the boxiest object in Fig. 5a, but is seen in Fig. 5b to exhibit only moderate ellipticity.

To restate the main result of this analysis: we find that galaxies with dusty disks exhibit a correlation between their average isophotal boxiness and the inclination of the disk with respect to the sky. Face-on disks are observed in round galaxies while edge-on disks are seen only in boxy galaxies. Furthermore, we observe a relationship between disk inclination and ellipticity that holds more strongly for objects with low or moderately inclined disks than it does for those with edge-on disks. In the following, we will make use of the latter result to explore the connections between the properties of the galaxies that possess lanes and their orientation.

#### 4.4. Estimating orientations of objects with dust lanes

To provide sample-wide context, in Fig. 6a we plot  $\epsilon_{\text{ave}}$  versus  $(a_4/a)_{\text{ave}}$  for the whole sample. Filled squares represent

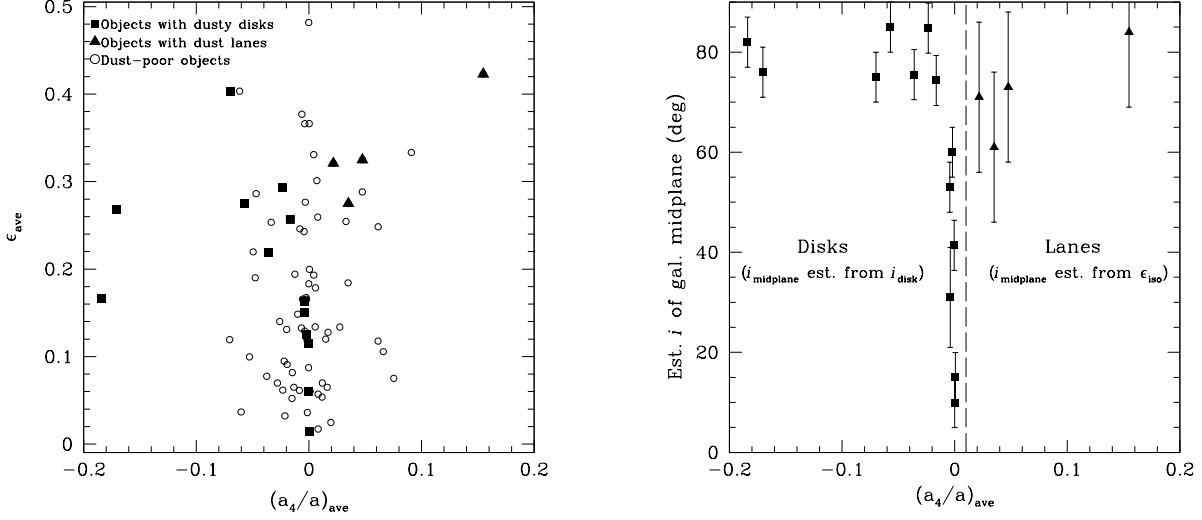


FIG. 6.— (a) Average ellipticity  $\epsilon_{\text{ave}}$  vs. average isophotal boxiness  $(a_4/a)_{\text{ave}}$  for each object in our sample. (b) A qualitative estimation of the inclination  $i_{\text{midplane}}$  (in degrees, with respect to the plane of the sky) of the galactic midplanes of the dust-rich host galaxies in our sample. For hosts containing disks (which are expected to reside in a symmetry plane), we estimate  $i_{\text{midplane}}$  directly by disk inclination. For hosts containing lanes, we estimate  $i_{\text{midplane}}$  based on the loose ellipticity-disk inclination relationship apparent in Fig. 5b (and discussed in §5), as well as qualitative appearance. The figure is intended to illustrate the apparent bimodality in isophotal structures of disk- and lane-containing hosts.

objects with dusty disks, filled triangles are objects with dust lanes, and empty circles are “dust poor” galaxies. Despite the fact that objects with extreme values of  $|(a_4/a)_{\text{ave}}|$  are present, our sample is clearly clustered around small values of  $|(a_4/a)_{\text{ave}}|$ . However, we stress that even a small difference in  $|(a_4/a)_{\text{ave}}|$  between two galaxies implies a significant difference in the structure of their respective isophotes. As we move to bins of greater degrees of boxiness (leftward on the  $(a_4/a)_{\text{ave}}$  axis of Fig. 6a), the fraction of bins occupied by objects with dusty disks roughly increases proportionately. While roughly 25% of the bin centered around  $(a_4/a)_{\text{ave}} = 0$  consists of hosts with dusty disks, 100% of the boxiest bins contain disks. Note also that the four objects with lanes are all located in the top right-hand-corner of the plot. This means that lanes are present in galaxies with both disky and high ellipticity isophotes. In §4.3 we found a trend between ellipticity and orientation of the dusty disks. Since those disks are closely aligned with the major axis of the galaxies in which they reside (Tran et al. 2001), it is tempting to derive an “orientation” for the galaxies with lanes.

In Fig. 6b we present a plot to extend that of Fig. 5a to include the lanes, for which we plot large error bars due to the uncertainty in the inclination-ellipticity relation. While on the left side of the plot both high and low inclination disks are present, on the right side we lack low ellipticity galaxies with lanes. With only 4 galaxies in the sample it is difficult to establish whether this is due to a selection bias or it is a real effect. Regardless, this figure serves to again illustrate that lanes are observed only in disky hosts, as well as suggests at a possible dependence of diskiness on midplane inclination, just as we observe for our larger sample of dusty disks in boxy galaxies.

#### 4.5. Comparison of isophotes with radio luminosities and core-dominance ratios

In Fig. 7a we plot the sample-wide distribution of total radio luminosities at 178 MHz (retrieved from the NASA/IPAC Extragalactic Database) against  $(a_4/a)_{\text{ave}}$ , so as to explore

possible connections between radio-loudness and isophotal structure. We observe no apparent trend as there is fairly heavy scatter, though we note that FR Is with dusty disks exclusively occupy the low-power end (left-hand side) of the plot, while dust-poor FR Is are spread across the whole range.

Galaxies whose radio emission is dominated by the core at 5 GHz imply a measure of beaming of the radio jet, while observations dominated by emission at 178 MHz suggests that the viewer is observing unbeamed, more edge-on jet lobes. The core-dominance ratio  $R$  of core (5 GHz) to extended region (178 MHz) fluxes is therefore a rough orientation indicator of the line of sight with respect to the central AGN. We plot  $(a_4/a)_{\text{ave}}$  vs.  $R$  in Fig. 7b by division of core flux at 5 GHz by the total 178 MHz flux. Again, we observe no trend in this figure given the scatter. We do note that NGC 6251, the bottom-most black triangle in Fig. 7b, is highly core-dominated, but is the boxiest object in our sample with a nearly edge-on dusty disk in its nucleus. While this would normally be surprising, the disk in NGC 6251 has been modeled with a warp, such that the outer regions of the disk are edge-on and aligned with the isophotal major axis of the galaxy, while the inner accretion region is oriented such that the jet is roughly pointed toward the observer, accounting for the apparent discrepancy (e.g., Ferrarese & Ford 1999; Chiaberge et al. 2003).

In both Figs. 7a and b we use triangles to denote FR I galaxies and circles to denote FR II galaxies. Empty symbols indicate that the object is “dust-poor”, and black symbols mark the presence of a dusty disk. Bold empty circles indicate an FR II in which we observe a lane. We do not observe any lanes in FR I galaxies. We also note that, while powerful, edge-brightened FR II galaxies outnumber the low-power, edge-darkened FR Is in our sample by over 2:1, we find that dusty disks reside in over twice as many FR I galaxies as in FR IIs. Moreover, all of the dust lanes in our sample are found in FR II hosts. This is consistent with the findings of de Koff et al. (2000), who noted that dust in FR I galaxies is typically found in the form of a nuclear disk below 2.5 kpc in size, while FR

IIs more commonly possess dust in clumpy patches and filaments. While these results are interesting, we must be wary of a possible observational bias, as FR II galaxies are typically found at higher redshifts than FR Is.

### 5. IMPLICATIONS OF OUR RESULTS

In §4.3 we describe an apparent relationship between the inclinations of circumnuclear dusty disks in our sample and the boxiness of their host galaxy isophotes. We observe that edge-on dusty disks reside in boxy host galaxies, while face-on disks are seen only in round galaxies. Intermediately inclined disks reside in more elliptical galaxies. Dust lanes, on the other hand, are only found in hosts with moderate to high levels of diskiness. Dusty disks reside in 13 of the 33 objects with dust observed in varying distributions through *HST*/WFPC2 optical imaging. These 33 objects are a subset of our 84 object sample with *HST*/NIC2 near-infrared imaging. Our sample of hosts possessing dusty disks is free from orientation bias (see §2) and we find no exceptions to the apparent inclination-boxiness trend described above. Martel et al. (2000) noticed a similar trend in their optical study of 7 of the dusty disks we describe here. In our sample, nearly twice as large as that of Martel et al. (2000), the trend has only grown stronger and more convincing. In this section, we argue that our results carry interesting implications with regards to the manifestation of isophotal structure, as well as the post-merger history of dust in the settling sequences of boxy and disk galaxies.

#### 5.1. Is boxiness dependent on viewing angle?

Here we discuss whether or not our results suggest that boxiness is an orientation-dependent effect. It is evident from Figs. 5 and 6 that nearly edge-on dusty disks reside in boxy galaxies that span an order of magnitude in values of  $(a_4/a)_{\text{ave}}$ . Conversely, the moderate- to low-inclination disks are seen only in host galaxies with very similar values of  $(a_4/a)_{\text{ave}}$ , all of which are nearly zero (though all are just slightly negative). The fact that such tight clustering is absent for the highly inclined disks may reflect intrinsic differences in the stellar velocity dispersions of these galaxies, as varying degrees of velocity anisotropy and orbital triaxiality are thought to produce varying degrees of boxiness (e.g., Bender 1988; Hao et al. 2006).

We may associate the inclinations of dusty disks with the inclinations of the galactic midplanes in which they are expected to settle. The rotation axis of the disk is therefore aligned with a symmetry axis of the underlying galaxy. Keeping this in mind and considering both Figs. 5a and b together, a qualitative picture of the possible dependence of boxiness on viewing angle begins to emerge. Were we to view a test galaxy with a line-of-sight coincident to its symmetry axis, we would view its perpendicular midplane as face-on. As the inclination of the symmetry axis with respect to the line-of-sight increases to more moderate levels, Figs. 5a and b suggest that perceived boxiness would remain nearly nonexistent, while isophotal ellipticity would increase significantly with the change in viewing angle. Only when we are viewing the galaxy's symmetry axis nearly in the plane of the sky (such that the galactic midplane is edge-on) may boxiness become fully apparent in the isophotes. For example, if we were somehow able to view the face-on disk in 3C 66B as edge-on, the otherwise round isophotes of its host might appear boxy.

Our sample is randomly oriented, and there is no reason to expect that face-on disks and edge-on disks reside in different populations of galaxies. We therefore conclude that boxi-

ness is, at least in part, an orientation-dependent phenomenon. This is consistent with the results of early *N*-boxy simulations of galaxy mergers, which found that the boxiness of a remnant is dependent on viewing angle (e.g., Lima Neto & Combes 1995). It is tempting to surmise that such an orientation dependence extends to disk isophotes, as well. The four dust lanes in our sample are found only in disk galaxies, though this small number prevents us from drawing conclusions from their already uncertain distribution in Fig. 6b. Past simulations of mergers that account for gas dissipation suggest that our results have relevance with regards to the role of dust as a tracer of merger history, which we discuss this below.

#### 5.2. Dust as a tracer of merger history

Here we qualitatively discuss the implications of our results with respect to the role of gas dynamics in the formation of boxy and disk merger remnants. It is clear that there is an intrinsic connection between the morphology and inclination of dust and the isophotal structure of the early type host in which it resides. Hardly a new idea, such a connection is expected on at least a theoretical level. Gas and dust acquired through a cannibalistic merger should coalesce on a few dynamical timescales and precess in a symmetry plane of the newly formed remnant, finally settling into the potential well of the host on a precession timescale (e.g., Gunn 1979; Tubbs 1980; Tohline et al. 1982; Habe & Ikeuchi 1985). All of this should occur on a timescale of order a Gyr, during which time the dust should dissipate angular momentum at a rate dependent upon the structure of the potential well and the star formation efficiency of the gas (Barnes 1996; Bekki & Shioya 1997). In the scenario proposed by Lauer et al. (2005), filamentary distributions of dust that have not yet reached the nucleus would be classified as dust lanes, which might be thought of as transient structures that would eventually form a nuclear disk if given sufficient time.

Dynamically, the presence of added gas and dust in the central potential is thought to alter the shape of the well, causing destabilization in central stellar box orbits and thus affecting the structure of the host galaxy's isophotes (Barnes 1996). This is supported by numerous simulations of dissipational mergers, which find that higher gas/dust content in one or both of the progenitor galaxies typically leads to more pronounced diskiness in the remnant (e.g., Springel 2000, and references therein). On the other hand, boxy galaxies are formed through gas-poor mergers of progenitors with high-density stellar bulges of relatively equal mass (e.g., Nabb & Burkert 2003; Khochfar & Burkert 2005).

Our results are consistent with the notion that dust acquired through a merger has a direct impact on the manifestation of boxiness or diskiness in the remnant. We find, however, that the nuclear dusty disks in our sample are exclusively associated with either boxy, elliptical, or round hosts, and are never observed in disk galaxies, which are seen only to contain dust lanes. This seems contrary to the idea that dust-rich (“wet”) mergers produce disk remnants *if we hold that disks and lanes are both external in origin*. In that case, the presence of a disk indicates that a large portion of externally acquired dust has been allowed to settle in the nucleus following the merger, thereby disrupting stellar box orbits and washing out isophotal boxiness (according to theory and simulations).

We observe the opposite to be true, finding that the circumnuclear dusty disks in our sample exclusively prefer boxy hosts. Recall that the 3CR sample should be free from orientation bias, and that the total  $(a_4/a)_{\text{ave}}$  distribution of our



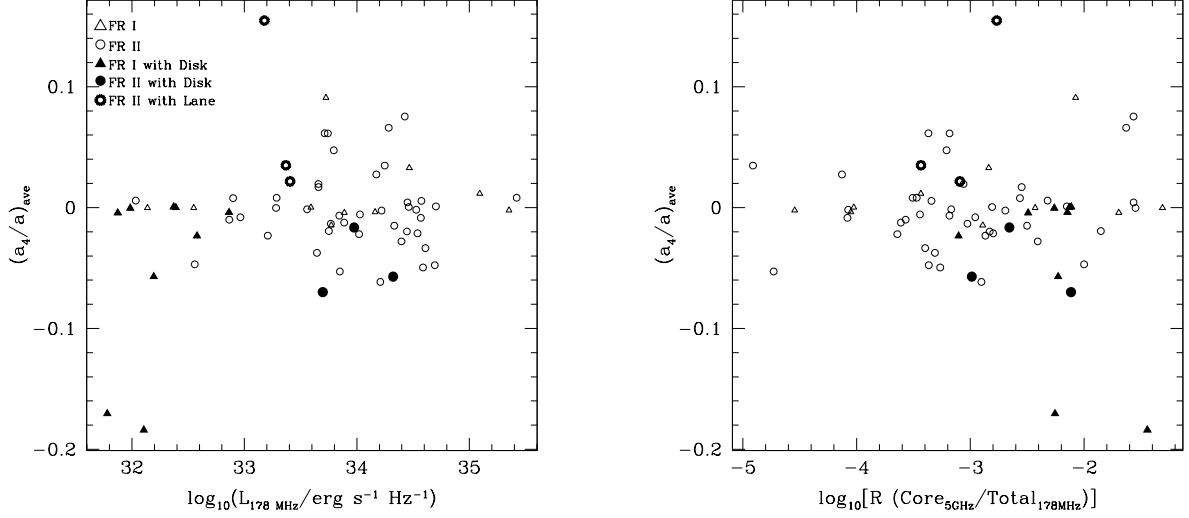


FIG. 7.— (a) Average isophotal boxiness vs. the log of the total radio luminosity at 178 MHz (values taken from NED). (b) The same boxiness distribution in (a) vs. 5 GHz / 178 MHz core-dominance ratios  $R$ . More core-dominated galaxies (like NGC 6251, the lowest black triangle in the plot) are closer to the right edge of the figure.

84 targets is largely isotropic, (e.g., while the majority of our sample is boxy, nearly one-third of our targets would qualify as disk; see Fig. 4). Were there not *some* intrinsic preference for boxiness among the population containing nuclear disks, it is statistically likely that we would have found dusty disks in a few disk hosts. Instead, dust-rich disk ellipticals in our sample only possess dust in the form of lanes.

Our results might be reconciled with those of past simulations if we consider a scenario in which dusty disks and lanes have distinct origins. This has been suggested before, based on the observed tendency for dusty disks, not lanes, to align with the isophotes of their hosts (Tran et al. 2001). That study offered a possible explanation, which our results support:

- Dusty disks are *native* to the nucleus of a progenitor galaxy with a high-density stellar core. In an equal-mass merger destined to produce a boxy remnant (as predicted by simulations), this dust remains in the nucleus of the parent, and any perturbations it experiences vanish rapidly. In this scenario, dusty disks are ancient structures, and are comprised of dust that has resided in the nucleus of a massive progenitor *prior* to the last merger event.
- Filamentary dust lanes are truly *external* in origin, and are the product of tidal stripping or the recent collision of small, unequal mass, gas-rich progenitors with significant dust mass residing in the outer extents of their volumes. In the disk remnant, rapid stellar rotation and an ISM recently shocked by the collision prevent the newly acquired dust from efficiently losing angular momentum. Instead of settling into the nucleus, it is distributed in a filamentary fashion at more distant radii. This would be consistent with findings that lanes do not typically align with the major axis of their host, while the opposite is true for dusty disks.

Our results are consistent with those of previous studies in suggesting that the elliptical hosts of nuclear dusty disks and lanes are drawn from two different galaxy populations with distinct formation histories. We conclude that disks reside in

old remnants of gas-free “dry” mergers, while lanes primarily reside in young remnants of gas-rich “wet” mergers. This comprises the second main conclusion of this paper.

## 6. SUMMARY AND DISCUSSION

In this paper we have examined possible connections between the morphology of dust distributions in radio galaxies and the isophotal properties of their elliptical hosts. We obtain deep near-infrared *HST*/NIC2 and *TNG* imaging of a sample of 84 radio galaxies, the majority of which are found in the 3CR catalog of extragalactic sources. For a 33 object subset of our sample identified as dust-rich by previous *HST* optical studies, we retrieve companion *HST*/WFPC2 *R*-band imaging of the nuclear regions of each host. We create *H/R*-band NIC2/WFPC2 color-maps for each dusty host so as to more clearly resolve the dust features contained within. Among our dust-rich subset, we identify 13 circumnuclear dusty disks and 4 filamentary lanes, while the remaining dust-rich hosts possess dust in less settled distributions like clumps and patches. From the luminosity profiles extracted from the near-infrared images of each galaxy in our sample, we qualitatively select radial regions over which we calculate the isophotal structural metrics  $(a_4/a)_{\text{ave}}$  (the average Fourier boxiness coefficient) and  $\epsilon_{\text{ave}}$  (the average ellipticity of the isophotes).

This allows for a comparison between the distribution of the dust features in our sample and the isophotal boxiness and ellipticity of the hosts in which they are found. Among those objects containing dusty disks and lanes, we find the following:

- Edge-on (with respect to the line of sight) dusty disks are seen only in host galaxies with boxy isophotes (e.g.,  $(a_4/a)_{\text{ave}} < 0$ ; see Fig. 5a).
- Face-on dusty disks are seen only in host galaxies with nearly round isophotes (e.g.,  $(a_4/a)_{\text{ave}} \approx 0$ , low  $\epsilon_{\text{ave}}$ , see Figs. 5a and b).
- Intermediately-inclined dusty disks are seen in host galaxies with elliptical isophotes (e.g.,  $(a_4/a)_{\text{ave}} \approx 0$ , intermediate  $\epsilon_{\text{ave}}$ , see Figs. 5a and b).

- Dust lanes are seen exclusively in disky host galaxies (e.g. with pointed isophotes,  $(a_4/a)_{\text{ave}} > 0$ ).
- No disky host galaxies are observed to contain dusty nuclear disks.

We discuss these results in the context of the role of dust in the formation of boxy and disky merger remnants. While our sample of 13 dusty disks is relatively small, we argue that the connection they share with the isophotes of their hosts carry real implications as to the expression of isophotal structure and the post-merger histories of dusty disks and lanes. In §5, we discuss how our results corroborate those of previous studies in suggesting that:

1. Isophotal boxiness is dependent on viewing angle. When viewed along the galactic axis of symmetry, the dusty disks in our sample are face-on and the isophotes of the host are round. When the axis of symmetry is highly inclined with respect to the line-of-sight, the disks are nearly edge-on and the isophotes appear boxy. We have no reason to suspect that the high and low inclination dusty disks are residing in different populations of galaxies. The degree of perceived boxiness in this galaxy population (e.g., those that host dusty disks) must therefore be dependent on viewing angle.
2. Dusty disks may not be external in origin as previously thought. Instead, they may be long-time residents of old gas-free merger remnants with high degrees of stellar velocity anisotropy accounting for intrinsic (though not necessarily observed) boxiness.
3. Filamentary dust lanes might share an entirely distinct history, having been acquired through recent gas-rich dissipative mergers of low-mass progenitors. The higher degree of isotropic stellar rotation that gives rise to the disky isophotes of this population might account for the fact that we only see lanes in disky hosts. Dust in a rapidly rotating system is less able to lose angular momentum effectively, greatly lengthening its lifetime as a filamentary lane.

The study of dust and host galaxy isophotal properties helps to place constraints on the dynamics of early-type stellar components and their associated potentials. By extension, these may contain information relating to the angular momentum of the last major merger, which might play a dominant role in the carving of galactic equipotentials and in setting the spin axis of the central black hole. In this regard, dust might act as an observable gauge of otherwise inobservable connections between AGN and the properties of their host galaxies.

The results of this paper illustrate such a possible relationship, and even more examples are found within our own sample. 3C 236, for instance, is unique in that it contains both an inner dusty disk and an outer dust filament only partially connected to the inner dust structure (Fig. 8). O’Dea et al. (2001) explored the relationship between the radio activity of 3C 236 and its dust morphology. That study suggested that the AGN fuel supply had been cut off at some time in the past, and AGN activity has only recently resumed, accounting for its relatively young radio morphology. The isophotes of 3C 236, while boxy, are also highly elliptical and irregularly shaped, suggesting that it has recently undergone a merger event, a notion supported by its disturbed outer dust features.

Another example of dust serving to illustrate connections between an AGN and its host galaxy is found in 3C 449, a clear outlier to the observed (though not necessarily real) jet/disk orthogonality “trend” discussed in §1 (see Fig. 8). The outer regions of the dusty disk are aligned with the isophotal major axis of the host, which makes a sharply acute angle with the radio jet axis on the plane of the sky. The recent work by Tremblay et al. (2006) modeled the dusty disk with a large warp, accounting for jet/disk orthogonality on smaller ( $\sim 50$  pc) scales. That study discussed physical mechanisms capable of creating and/or sustaining such a warp, concluding that its source most likely comes from a perturbative interaction between the dusty disk and highly elongated, anisotropically distributed isobars of X-ray emitting gas in the ambient medium. Were such anisotropy coupled to the launching of the jet through a feedback interaction from the AGN, it may play a large role in a process responsible for preferentially aligning dusty disks to radio jets, accounting for jet/disk orthogonality.

Indeed, recent observations have revealed the interstellar media in the central few hundred pc of many radio galaxies to be highly turbulent and capable of perturbing equilibrium morphologies of the dust in these areas (e.g., Fabian et al. 2003; Noel-Storr et al. 2003; Vernaleo & Reynolds 2006). The study of dust in relation to AGN feedback processes might help account for observed non-equilibrium dust morphologies like tendrils and warps that should otherwise be short-lived. In a hot ISM lacking a cold counterpart, erosive processes might even be capable of destroying the dust altogether through sputtering (e.g., Canizares, Fabbiano, & Trinchieri 1987; Dwek & Arendt 1992). Future studies will further our understanding of the morphological evolution of dust, as well as the ultimate longevity of this dust in highly energetic environments like the hearts of radio galaxies.

To that end, it is necessary that we expand on this work to include larger samples of radio galaxies as well as non-active elliptical populations. More sophisticated comparisons between isophotal, dusty disk, and radio jet axes may yet reveal a deeper connection between these structures than was previously thought to exist. Furthermore, the understanding of dust in radio-loud unification models may be crucial to probing the divides between FR I and II-type radio galaxies, and whether these two classes reflect stages of an evolutionary sequence, or are intrinsically distinct objects altogether.

We are grateful to Stefi Baum, David Floyd, and Andrew McCullough for helpful discussions. We also thank William Keel, our referee, whose feedback led to the improvement of this paper. This work is based on observations made with the NASA/ESA *Hubble Space Telescope*, obtained at the Space Telescope Science Institute, which is operated by the Association of Universities for Research in Astronomy, Inc., under contract NAS 5-26555 with the National Aeronautics and Space Administration. Support for this work was provided by NASA through grant HST-GO-10173. This research made extensive use of the NASA Astrophysics Data System Bibliographic services, as well as the NASA/IPAC Extragalactic Database, operated by the Jet Propulsion Laboratory, California Institute of Technology, under contract with NASA.

## REFERENCES

- Bardeen, J. M., & Petterson, J. A. 1975, *ApJ*, 193, L65
- Barnes, J. E. 1996, in *Proc. IAU Symp.* 171, Kluwer Academic Publishers, Ed. Bender, R., Davies, R. L., *New Light on Galaxy Evolution*, p. 191
- Bekki, K., & Shioya, Y. 1997, *ApJ*, 478, L17
- Bender, R. & Möllenhoff, C. 1987, *A&A*, 177, 71
- Bender, R. 1988, *A&A*, 193, L7
- Bender, R., Burstein, D., & Faber, S. M., 1992, *ApJ*, 399, 462
- Bennett, A.S. 1962a, *Mem. RAS*, 68, 163
- Bennett, A.S. 1962b, *MNRAS*, 125, 75
- Canizares, C. R., Fabbiano, G., & Trinchieri, G. 1987, *ApJ*, 312, 503
- Capetti, A., & Celotti, A. 1999, *MNRAS*, 304, 434
- Capetti, A., Celotti, A., Chiaberge, M., de Ruiter, H. R., Fanti, R., Morganti, R., & Parma, P. 2002, *A&A*, 383, 104
- Chiaberge, M., Capetti, A., & Celotti, A. 2002, *A&A*, 394, 791
- Chiaberge, M., Gilli, R., Capetti, A., & Macchetto, F. D. 2003, *ApJ*, 597, 166
- Cimatti, A. et al. 2004, *Nat*, 430, 184
- de Koff, S., Baum, S. A., Sparks, W. B., Biretta, J., Golombek, D., Macchetto, F., McCarthy, P., & Miley, G. K. 1996, *ApJS*, 107, 621
- de Koff, S., Best, P., Baum, S. A., Sparks, W., Rottgering, H., Miley, G., Golombek, D., Macchetto, F., & Martel, A. 2000, *ApJS*, 129, 33
- de Ruiter, H. R., Parma, P., Capetti, A., Fanti, R., & Morganti, R. 2002, *A&A*, 396, 857
- Donzelli, C. J., Macchetto, F. D., Chiaberge, M., Madrid, J. P., Sparks, W. B., Capetti, A., & Marcesini, D. 2007, in preparation (astro-ph/0612546)
- Dwek, E. and Arendt, R. G. 1992, *ARA&A*, 30, 11D
- Faber, S. et al. 1997, *AJ*, 114, 1771
- Fabian, A. C., Sanders, J. S., Allen, S. W., Crawford, C. S., Iwasawa, K., Johnstone, R. M., Schmidt, R. W., & Taylor, G. B. 2003, *MNRAS*, 344, 43
- Fanaroff, B. L. & Riley, J. M. 1974, *MNRAS*, 167, 31p
- Ferrarese, L., van den Bosch, F. C., Ford, H. C., Jaffe, W., & O'Connell, R. W. 1994, *AJ*, 108, 1598
- Ferrarese, L., Ford, H. C., & Jaffe, W. 1996, *ApJ*, 470, 444
- Ferrarese, L., & Ford, H. C. 1999, *ApJ*, 515, 583
- Ferrari, F., Pastoriza, M. G., Macchetto, F., & Caon, N. 1999, *A&AS*, 136, 269
- Floyd, D. J. E., Perlman, E., Leahy, J. P., Beswick, R. J., Jackson, N. J., Sparks, W. B., Axon, D. J. & O'Dea, C. P. 2006, *ApJ*, 639, 23
- Forbes, D. A. 1991, *MNRAS*, 249, 779
- Fraix-Burnet, D., Golombek, D., & Macchetto, F. D. 1991, *AJ*, 102, 562
- Goudfrooij, P., 1994a, Ph.D. thesis, Amsterdam
- Goudfrooij, P. et al. 1994, *A&AS*, 105, 341
- Goudfrooij, P., & de Jong, T. 1995, *A&A*, 298, 784
- Gunn, J. E. 1979, in *Active Galactic Nuclei*, ed. C. Hazard & S. Mitton (Cambridge: Cambridge Univ. Press), 213
- Habe, A., & Ikeuchi, S. 1985, *ApJ*, 289, 540
- Hao, C. N., Mao, S., Deng, Z. G., Xia, X. Y. & Hong Wu 2006, *MNRAS*, 370, 1339
- Hernquist, L. 1993, *ApJ*, 409, 548
- Jaffe, W., Ford, H., Ferrarese, L., van den Bosch, F. C., & O'Connell, R. W. 1996, *ApJ*, 460, 214
- Jedrzejewski, R. 1987, *MNRAS*, 226, 747
- Khochfar, S., & Burkert, A. 2005, *MNRAS*, 359, 1379
- Kotanyi, C., & Ekers, R. 1979, *A&A*, 73, L1
- Kumar, S., & Pringle, J. E. 1985, *MNRAS*, 213, 435
- Laing, R. A., Riley, J. M., & Longair, M. S. 1983, *MNRAS*, 204, 151
- Lauer, T. R. et al. 1995, *AJ*, 110, 2622
- Lauer, T.R. et al. 2005, *AJ*, 129, 2138
- Lima Neto, G. B., Combes, F. 1995, *A&A*, 294, 657
- Madrid, J. P. et al., 2006, *ApJS*, 164, 307
- Marchesini, D., Capetti, A., & Celotti, A. 2005, *A&A*, 433, 841
- Martel, A., et al. 1999, *ApJS*, 122, 81
- Martel, A., Turner, N., Sparks, W., Baum, S. 2000, *ApJS*, 130, 267
- Milvang-Jensen, B., & Jørgensen, I. 1999, *Baltic Astronomy*, 8, 535
- Möllenhoff, C., Hummel, E., & Bender, R. 1992, *A&A*, 255, 35
- Naab, T., & Burkert, A. 2003, *ApJ*, 597, 893
- Noel-Storr, J., Baum, S. A., Verdoes Kleijn, G., van der Marel, R. P., O'Dea, C. P., de Zeeuw, P. T., & Carollo, C. M. 2003, *ApJS*, 148, 419
- Noel-Storr, J. et al. 2007, in preparation
- Noll, K., et al. 2004, *NICMOS Instrument Handbook*, Version 7.0, (Baltimore, STScI)
- O'Dea, C. P., Koekemoer, A. M., Baum, S. A., Sparks, W. B., Martel, A. R., Allen, M. G., Macchetto, F. D., & Miley, G. K. 2001, *AJ*, 121, 1915
- Quillen, A. C., & Bower, G. 1999, *ApJ*, 522, 718
- Quillen, A. C. 2001, *ApJ*, 563, 313
- Rees, M. J., Begelman, M. C., Blandford, R. D., & Phinney, E. S. 1982, *Nature*, 295, 17
- Rix, H., & White, S. D. M. 1990, *ApJ*, 362, 52
- Sadler, E. M., & Gerhard, O. E. 1985, *MNRAS*, 214, 177
- Scorza, C., & Bender, R. 1995, *A&A*, 293, 20
- Schmitt, H. R., Pringle, J. E., Clarke, C. J., & Kinney, A. L. 2002, *ApJ*, 575, 150
- Schilizzi, R. T., Tian, W. W., Conway, J. E., Nan, R., Miley, G. K., Barthel, P. D., Normandeau, M., Dallacasa, D. & Gurvits, L. I. 2001, *A&A*, 368, 398
- Searle, L., Sargent, W. L. W., & Bagnuolo, W. G., 1973, *ApJ*, 179, 427
- Sparks, W. B., Baum, S. A., Biretta, J., Macchetto, F. D., & Martel, A. R. 2000, *ApJ*, 542, 667
- Spinrad, H., Djorgovski, S., Marr, J., & Aguilar, L. 1985, *PASP*, 97, 932
- Springel, V. 2000, *MNRAS*, 312, 859
- Steiman-Cameron, T. Y., & Durisen, R. H. 1988, *ApJ*, 325, 26
- Tohline, J. E., Simonson, G. F., & Caldwell, N. 1982, *ApJ*, 252, 92
- Tomita, A., Aoki, K., Watanabe, M., Takata, T., & Ichikawa, S., 2000, *AJ*, 120, 123
- Toomre, A. & Toomre, J. 1972, *ApJ*, 178, 623
- Tran, H. D., Tsvetanov, Z., Ford, H. C., & Davies, J. 2001, *AJ*, 121, 2928
- Tremblay, G. R., Quillen, A. C., Floyd, D. J. E., Noel-Storr, J., Baum, S., Axon, D., O'Dea, C. P., Chiaberge, M., Macchetto, F. D., Sparks, W. B., Miley, G. K., Capetti, A., Madrid, J. P., & Perlman, E. 2006, *ApJ*, 643, 101
- Tubbs, A. D. 1980, *ApJ*, 241, 969
- van den Bosch, F. C., Ferrarese, L., Jaffe, W., Ford, H. C., & O'Connell, R. W. 1994, *AJ*, 108, 1579
- van Dokkum, P. D., & Franx, M. 1995, *AJ*, 110, 2027
- Verdoes Kleijn, G. A., Baum, S. A., de Zeeuw, P. T., & O'Dea, C. P. 1999, *AJ*, 118, 2592
- Verdoes Kleijn, G. A., & de Zeeuw, P. T. 2005, *A&A*, 435, 43
- Vernaleo, J. C., & Reynolds, C. S. 2006, *ApJ*, 645, 83
- Véron-Cetty, M.-P., & Véron, P. 1988, *A&A*, 204, 28
- Waggett, P. C., Warner, P. J., & Baldwin, J. E. 1977, *MNRAS*, 181, 465

TABLE 1  
HOST GALAXY ISOPHOTAL PROPERTIES AND DUST DISTRIBUTIONS

| Source<br>(1) | $(a_4/a)_{\text{ave}}$<br>(2) | $\epsilon_{\text{ave}}$<br>(3) | $z$<br>(4) | $n$<br>(5) | $r_e/\text{kpc}$<br>(6) | $m_e$<br>(7) | Isophote Morphology<br>(8) | Dust Morphology<br>(9)     | Reference<br>(10) |
|---------------|-------------------------------|--------------------------------|------------|------------|-------------------------|--------------|----------------------------|----------------------------|-------------------|
| 3C 17         | 0.004313                      | 0.19                           | 0.21968    | 0.370      | 3.21                    | 18.28        | Elliptical                 | —                          | 1                 |
| 3C 20         | -0.06019                      | 0.03                           | 0.17400    | 0.350      | 2.33                    | 17.89        | Boxy                       | Thin tendril               | 1,2               |
| 3C 28         | 0.034791                      | 0.18                           | 0.19520    | 0.821      | 1.05                    | 17.76        | Disk                       | —                          | 1                 |
| 3C 31         | -0.00041                      | 0.11                           | 0.01670    | 0.272      | 5.22                    | 18.09        | Elliptical                 | Disk incl. $\sim 41^\circ$ | 1,2               |
| 3C 33.1       | -0.03744                      | 0.07                           | 0.18090    | 0.443      | 3.08                    | 18.65        | Boxy                       | —                          | 1                 |
| 3C 35         | 0.007849                      | 0.26                           | 0.06700    | 0.371      | 5.89                    | 18.77        | Elliptical                 | —                          | 1                 |
| 3C 52         | 0.007006                      | 0.30                           | 0.28540    | 0.240      | 8.34                    | 19.06        | Elliptical                 | Thin tendril               | 1,2               |
| 3C 61.1       | -0.001803                     | 0.12                           | 0.18400    | 0.282      | 2.86                    | 19.52        | Elliptical                 | —                          | 1                 |
| 3C 66B        | 2.519e-06                     | 0.06                           | 0.02150    | 0.248      | 9.16                    | 19.31        | Round                      | Face-on Disk               | 1,2,3             |
| 3C 75N        | -0.000145                     | 0.18                           | 0.02315    | 0.247      | 1.98                    | 17.10        | Round                      | —                          | 1                 |
| 3C 76.1       | -0.002024                     | 0.13                           | 0.03240    | 0.261      | 1.08                    | 16.70        | Round                      | Face-on Disk               | 1,3               |
| 3C 79         | -0.047640                     | 0.19                           | 0.25595    | 0.348      | 4.27                    | 18.38        | Boxy                       | —                          | 1                 |
| 3C 83.1       | -0.023451                     | 0.29                           | 0.02550    | 0.214      | 12.01                   | 18.93        | Boxy                       | Edge-on Disk               | 1,2               |
| 3C 84         | $\sim -0.01$                  | 0.22                           | 0.01756    | 0.356      | 6.52                    | 18.73        | —                          | Complex patches            | 1,2               |
| 3C 88         | -0.046897                     | 0.29                           | 0.03022    | 0.227      | 4.92                    | 19.18        | Boxy                       | Very thin, faint tendril   | 1,2               |

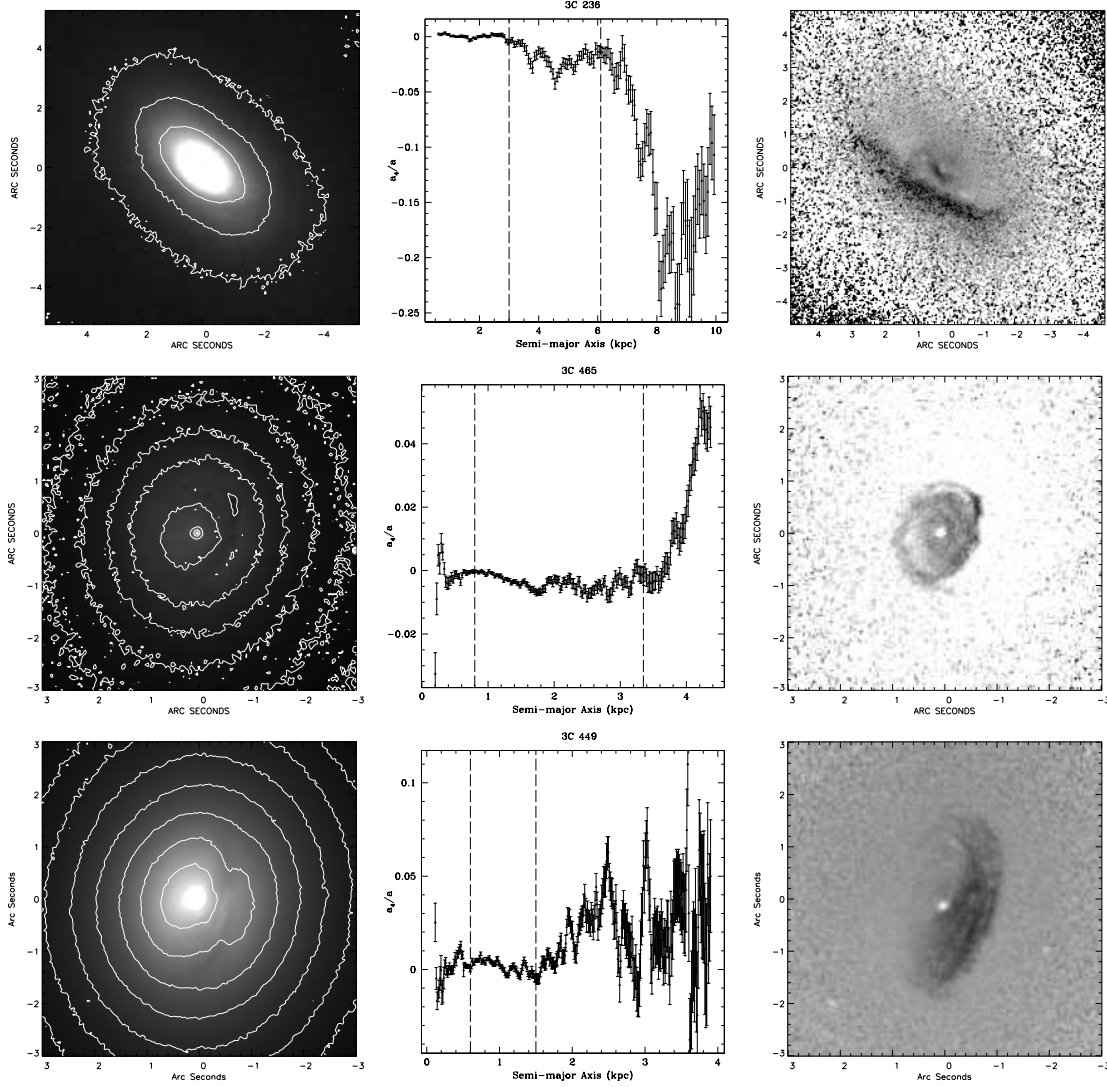


FIG. 8.— Examples of some of the unique dust features in our sample, which we discuss directly in §5. (Top) *HST*/NIC2  $1.6 \mu\text{m}$  image of 3C 236 with highlighted isophotal contours, its associated  $a_4/a$  radial profile with the averaging region (see §3) bounded by dashed lines, and a  $1.6 \mu / 0.7 \mu\text{m}$  colormap of the dusty disk in the nucleus of 3C 236, made via division of *HST*/NIC2 and WFPC2 data. This object is unique in that it is one of the largest galaxies in the universe, and its nucleus contains both a dusty disk and a dust lane. (Middle) Same as (Top), but for 3C 465. The disk in 3C 465 is lopsided, with two sharp spiral features to the north and south. (Bottom) Same as (Top), but for 3C 449. The dusty disk in this object is unique in that it is a clear outlier to the observed (but perhaps not real) jet/disk orthogonality “trend”, which we discuss in §1. The disk in 3C 449 has been modeled by Tremblay et al. (2006) with a large warp, accounting for jet/disk orthogonality on smaller ( $\sim 50$  pc) scales.

TABLE 1 — *Continued*

| Source<br>(1) | $(a_4/a)_{\text{ave}}$<br>(2) | $\epsilon_{\text{ave}}$<br>(3) | $z$<br>(4) | $n$<br>(5) | $r_e/\text{kpc}$<br>(6) | $m_e$<br>(7) | Isophote Morphology<br>(8) | Dust Morphology<br>(9) | Reference<br>(10) |
|---------------|-------------------------------|--------------------------------|------------|------------|-------------------------|--------------|----------------------------|------------------------|-------------------|
| 3C 98         | -0.010021                     | 0.15                           | 0.03000    | 0.248      | 3.12                    | 18.31        | Boxy                       | —                      | 1                 |
| 3C 105        | $\sim -0.03$                  | 0.28                           | 0.08900    | 0.315      | 1.19                    | 17.16        | —                          | —                      | 1                 |
| 3C 111        | -0.00032                      | 0.09                           | 0.04850    | 0.173      | 3.44                    | 18.87        | Elliptical                 | —                      | 1                 |
| 3C 123        | 0.008141                      | 0.06                           | 0.21770    | 0.166      | 28.65                   | 22.28        | Elliptical                 | —                      | 1                 |
| 3C 129        | -0.02592                      | 0.14                           | 0.02080    | 0.637      | 1.75                    | 17.39        | Boxy                       | —                      | 1                 |
| 3C 129.1      | 0.016238                      | 0.06                           | 0.02220    | 0.900      | 1.76                    | 17.32        | Disk                       | —                      | 1                 |
| 3C 132        | -0.002463                     | 0.17                           | 0.21400    | 0.362      | 5.36                    | 18.66        | Elliptical                 | —                      | 1                 |
| 3C 133        | 0.000983                      | 0.06                           | 0.27750    | 0.319      | 4.74                    | 19.44        | Round                      | —                      | 1                 |
| 3C 135        | -0.012420                     | 0.19                           | 0.12530    | 0.223      | 1.19                    | 17.12        | Boxy                       | —                      | 1                 |
| 3C 153        | -0.052845                     | 0.10                           | 0.27700    | 0.259      | 1.28                    | 16.79        | Boxy                       | —                      | 1                 |
| 3C 165        | 0.005589                      | 0.13                           | 0.29570    | 0.241      | 9.23                    | 20.21        | Elliptical                 | —                      | 1                 |
| 3C 166        | 0.075364                      | 0.08                           | 0.24500    | 0.225      | 14.18                   | 21.49        | Disk                       | —                      | 1                 |
| 3C 171        | -0.008469                     | 0.06                           | 0.23840    | 0.305      | 4.21                    | 19.11        | Elliptical                 | Thin tendril           | 1,2               |
| 3C 173.1      | -0.049518                     | 0.22                           | 0.29210    | 0.162      | 9.01                    | 19.46        | Boxy                       | Offset thin tendril    | 1,2               |
| 3C 180        | -0.006289                     | 0.38                           | 0.22000    | 0.242      | 7.44                    | 20.00        | Elliptical                 | Faint, thin patch      | 1,2               |
| 3C 184.1      | 0.0614536                     | 0.25                           | 0.11820    | 0.904      | 0.59                    | 15.79        | Disk                       | —                      | 1                 |
| 3C 192        | 0.008136                      | 0.02                           | 0.05980    | 0.253      | 2.61                    | 17.84        | Elliptical                 | —                      | 1                 |
| 3C 196.1      | -0.003252                     | 0.28                           | 0.19800    | 0.337      | 2.41                    | 19.03        | Elliptical                 | Offset thin patch      | 1,2               |
| 3C 197.1      | -0.001396                     | 0.04                           | 0.13010    | 0.227      | 4.73                    | 19.42        | Elliptical                 | —                      | 1                 |

TABLE 1 — *Continued*

| Source<br>(1) | $(a_4/a)_{\text{ave}}$<br>(2) | $\epsilon_{\text{ave}}$<br>(3) | $z$<br>(4) | $n$<br>(5) | $r_e/\text{kpc}$<br>(6) | $m_e$<br>(7) | Isophote Morphology<br>(8) | Dust Morphology<br>(9)            | Reference<br>(10) |
|---------------|-------------------------------|--------------------------------|------------|------------|-------------------------|--------------|----------------------------|-----------------------------------|-------------------|
| 3C 198        | -0.070424                     | 0.12                           | 0.08150    | 0.292      | 3.50                    | 19.31        | Boxy                       | —                                 | 1                 |
| 3C 213.1      | 0.004274                      | 0.33                           | 0.19400    | 0.281      | 4.59                    | 18.95        | Elliptical                 | —                                 | 1                 |
| 3C 219        | 0.000479                      | 0.20                           | 0.17440    | 0.399      | 6.27                    | 18.92        | Elliptical                 | —                                 | 1                 |
| 3C 223        | -0.006622                     | 0.13                           | 0.13680    | 0.286      | 4.06                    | 18.71        | Elliptical                 | —                                 | 1                 |
| 3C 223.1      | 0.021664                      | 0.32                           | 0.10700    | 0.261      | 1.50                    | 16.99        | Disk                       | Dust Lane(s)                      | 1                 |
| 3C 227        | 0.061402                      | 0.12                           | 0.08610    | 0.235      | 2.93                    | 18.47        | Disk                       | —                                 | 1                 |
| 3C 234        | -0.027986                     | 0.07                           | 0.18500    | 0.433      | 2.78                    | 17.88        | Boxy                       | —                                 | 1                 |
| 3C 236        | -0.069899                     | 0.40                           | 0.10050    | 0.291      | 10.06                   | 19.57        | Boxy                       | Lane, Edge-on Disk                | 1,2,4             |
| 3C 264        | 0.000581                      | 0.01                           | 0.02172    | 0.671      | 1.52                    | 16.13        | Round                      | Face-on Disk                      | 1,2               |
| 3C 270        | -0.17046                      | 0.27                           | 0.00747    | —          | —                       | —            | Boxy                       | Edge-on Disk                      | 2                 |
| 3C 277.3      | -0.023183                     | 0.06                           | 0.08570    | 0.255      | 5.54                    | 19.11        | Boxy                       | —                                 | 1                 |
| 3C 284        | -0.021973                     | 0.09                           | 0.23900    | 0.213      | 6.13                    | 19.44        | Boxy                       | Thin filament                     | 1,2               |
| 3C 285        | -0.008023                     | 0.25                           | 0.07940    | 0.239      | 3.00                    | 18.63        | Elliptical                 | —                                 | 1                 |
| 3C 287.1      | 0.066047                      | 0.11                           | 0.21590    | 0.268      | 1.00                    | 16.24        | Disk                       | —                                 | 1                 |
| 3C 288        | -0.021296                     | 0.03                           | 0.24600    | 0.749      | 4.79                    | 18.94        | Boxy                       | —                                 | 1                 |
| 3C 293        | —                             | —                              | 0.04503    | —          | —                       | —            | Highly irregular           | Complex tendrils, lanes           | 1,2,5             |
| 3C 296        | -0.057085                     | 0.28                           | 0.02370    | 0.277      | 6.60                    | 17.97        | Boxy                       | Edge-on Disk                      | 1                 |
| 3C 300        | -0.033492                     | 0.25                           | 0.27000    | 0.299      | 4.92                    | 19.31        | Boxy                       | —                                 | 1                 |
| 3C 303        | -0.019399                     | 0.09                           | 0.14100    | 0.259      | 5.30                    | 18.93        | Boxy                       | —                                 | 1                 |
| 3C 305        | $\sim -0.003$                 | 0.35                           | 0.04164    | 0.224      | 2.58                    | 17.39        | Elliptical                 | Patches, tendrils                 | 1,2               |
| 3C 310        | 0.0329299                     | 0.25                           | 0.05350    | 0.285      | 2.56                    | 18.09        | Disk                       | —                                 | 1                 |
| 3C 314.1      | 0.000278                      | 0.37                           | 0.11970    | 0.408      | 4.44                    | 18.99        | Elliptical                 | —                                 | 1                 |
| 3C 315        | 0.091022                      | 0.33                           | 0.10830    | 0.252      | 1.39                    | 16.83        | Disk                       | —                                 | 1                 |
| 3C 317        | $\sim -0.01$                  | 0.30                           | 0.03446    | 0.434      | 1.63                    | 17.83        | Elliptical                 | Thin tendrils                     | 1                 |
| 3C 319        | 0.027407                      | 0.13                           | 0.19200    | 0.353      | 0.78                    | 16.40        | Disk                       | —                                 | 1                 |
| 3C 326        | 0.154769                      | 0.42                           | 0.08900    | 0.269      | 1.38                    | 17.13        | Disk                       | Lane                              | 1,2               |
| 3C 332        | -0.013333                     | 0.06                           | 0.15150    | 0.254      | 0.88                    | 15.94        | Boxy                       | —                                 | 1                 |
| 3C 338        | $\sim -0.001$                 | 0.28                           | 0.03035    | 0.474      | 12.86                   | 19.03        | Round                      | Tendrils, clumps                  | 1,2               |
| 3C 346        | -0.004300                     | 0.24                           | 0.16100    | 0.270      | 0.46                    | 14.90        | Elliptical                 | —                                 | 1                 |
| 3C 348        | -0.002189                     | 0.17                           | 0.15400    | 0.925      | 9.25                    | 19.58        | Elliptical                 | —                                 | 1                 |
| 3C 349        | -0.061500                     | 0.40                           | 0.20500    | 0.249      | 1.48                    | 17.27        | Boxy                       | —                                 | 1                 |
| 3C 353        | 0.019501                      | 0.02                           | 0.03043    | 0.251      | 1.85                    | 17.86        | Disk                       | —                                 | 1                 |
| 3C 357        | 0.047445                      | 0.29                           | 0.16700    | 0.238      | 5.29                    | 18.94        | Disk                       | Faint, thin tendril(s)            | 1,2               |
| 3C 379.1      | 0.011905                      | 0.07                           | 0.25600    | 0.225      | 2.77                    | 18.14        | Disk                       | —                                 | 1                 |
| 3C 381        | -0.005648                     | 0.17                           | 0.16050    | 0.264      | 1.56                    | 17.10        | Elliptical                 | —                                 | 1                 |
| 3C 386        | 0.014887                      | 0.12                           | 0.01700    | 0.226      | 3.38                    | 18.32        | Disk                       | —                                 | 1                 |
| 3C 388        | 0.016990                      | 0.13                           | 0.09100    | 1.227      | 2.21                    | 17.64        | Disk                       | —                                 | 1                 |
| 3C 401        | -0.019726                     | 0.13                           | 0.20104    | 0.310      | 1.17                    | 17.89        | Boxy                       | —                                 | 1                 |
| 3C 402        | 0.005824                      | 0.18                           | 0.02390    | 0.190      | 5.00                    | 18.85        | Elliptical                 | —                                 | 1                 |
| 3C 403        | 0.034994                      | 0.27                           | 0.05900    | 0.405      | 4.72                    | 18.01        | Disk                       | Lane                              | 1,2               |
| 3C 405        | —                             | 0.25                           | 0.05608    | 0.525      | 14.85                   | 20.01        | Irregular, obscured        | Complex, offset patch             | 1,2               |
| 3C 424        | -0.014721                     | 0.08                           | 0.12699    | 0.254      | 3.67                    | 19.38        | Boxy                       | —                                 | 1                 |
| 3C 430        | 0.0475771                     | 0.32                           | 0.05560    | —          | —                       | —            | Disk                       | Lane                              | 2                 |
| 3C 433        | -0.003694                     | 0.37                           | 0.10160    | 0.494      | 2.51                    | 17.90        | Elliptical                 | Patchy clumps                     | 1,2               |
| 3C 436        | -0.035997                     | 0.22                           | 0.21450    | 0.255      | 6.61                    | 19.12        | Boxy                       | Edge-on Disk                      | 1,2               |
| 3C 438        | 0.011698                      | 0.05                           | 0.29000    | 0.298      | 9.96                    | 19.86        | Disk                       | —                                 | 1                 |
| 3C 449        | -0.004330                     | 0.15                           | 0.01710    | 0.164      | 5.08                    | 19.01        | Elliptical                 | Warped disk incl. $\sim 40^\circ$ | 1,2,6             |
| 3C 452        | -0.016480                     | 0.27                           | 0.08110    | 0.276      | 3.83                    | 18.15        | Boxy                       | Edge-on Disk                      | 1,2               |
| 3C 459        | -0.000975                     | 0.12                           | 0.21990    | 0.430      | 0.81                    | 15.45        | Elliptical                 | —                                 | 1                 |
| 3C 465        | -0.003960                     | 0.16                           | 0.03030    | 0.311      | 3.92                    | 17.67        | Elliptical                 | Face-on Disk                      | 1,2               |
| NGC 6251      | -0.183990                     | 0.17                           | 0.02471    | —          | —                       | —            | Boxy                       | Edge-on Disk                      | 7                 |

REFERENCES. — (1) Donzelli et al. (2007); (2) de Koff et al. (2000); (3) Sparks et al. (2000); (4) O’Dea et al. (2001); (5) Floyd et al. (2006); (6) Tremblay et al. (2006); (7) Ferrarese & Ford (1999)

NOTE. — (1) Source name; (2) 4th order cosine coefficient of ELLIPSE fit normalized to the isophote semi-major axis  $a$ . Negative values of  $a_4/a$  are representative of boxy isophotes, whereas positive values indicate a disk profile; (3) Isophotal ellipticity averaged over the same region as in (2); (4) Host galaxy redshift; (5) Sérsic index of model; (6) Effective radius of model in kpc; (7) Effective host surface brightness in mag arcsec $^{-2}$ , normalized to  $H$ -band Vega magnitudes; (8) Qualitative isophotal morphology; (9) Qualitative description of dust content and distribution, where applicable. No entry indicates that the host is optically dust-poor. (“Face-on” and “Edge-on” is a strictly qualitative assertion); (10) References